

## Article

# The Preparation of Mn-Modified CeO<sub>2</sub> Nanosphere Catalysts and Their Catalytic Performance for Soot Combustion

Siyu Gao<sup>1</sup>, Di Yu<sup>2</sup>, Shengran Zhou<sup>1</sup>, Chunlei Zhang<sup>1</sup>, Lanyi Wang<sup>2</sup>, Xiaoqiang Fan<sup>1</sup>, Xuehua Yu<sup>1,\*</sup>   
and Zhen Zhao<sup>1,2,\*</sup>

<sup>1</sup> Institute of Catalysis for Energy and Environment, College of Chemistry and Chemical Engineering, Shenyang Normal University, 253# Huanghe North Street, Huanggu District, Shenyang 110034, China; gsy990328@163.com (S.G.); zhoushengran1997@163.com (S.Z.); zhangchunlei0423@163.com (C.Z.); fanxiaoqiang1986@126.com (X.F.)

<sup>2</sup> State Key Laboratory of Heavy Oil Processing, China University of Petroleum, 18#Fuxue Road, Chang Ping, Beijing 102249, China; yudii1127@163.com (D.Y.); wanglanyii@163.com (L.W.)

\* Correspondence: yuxuehua1986@163.com (X.Y.); zhenzhao@cup.edu.cn (Z.Z.)

**Abstract:** With the increasing stringency of environmental protection regulations, reducing the severe pollution caused by soot particles from diesel vehicle exhaust has become a widespread concern. Catalytic purification technology is currently an efficient method for eliminating soot particles, which needs to develop high-activity catalysts. This work uses a two-step hydrothermal method to synthesize MnO<sub>x</sub>/CeO<sub>2</sub> nanosphere catalysts, which have synergistic effects between manganese and cerium, and have high reactive oxygen species. Among them, the MnCe-1:4 catalyst represents the optimal catalytic activity, and the values of T<sub>10</sub>, T<sub>50</sub>, and T<sub>90</sub> are 289, 340, and 373 °C, respectively. On account of their simple synthetic procedure and low cost, the prepared MnO<sub>x</sub>/CeO<sub>2</sub> nanosphere catalysts have good prospects for practical applications.

**Keywords:** MnO<sub>x</sub>/CeO<sub>2</sub> nanospheres; soot combustion; catalysts



**Citation:** Gao, S.; Yu, D.; Zhou, S.; Zhang, C.; Wang, L.; Fan, X.; Yu, X.; Zhao, Z. The Preparation of Mn-Modified CeO<sub>2</sub> Nanosphere Catalysts and Their Catalytic Performance for Soot Combustion. *Processes* **2023**, *11*, 2902. <https://doi.org/10.3390/pr11102902>

Academic Editor: George Z. Kyzas

Received: 28 August 2023

Revised: 25 September 2023

Accepted: 28 September 2023

Published: 2 October 2023



**Copyright:** © 2023 by the authors. Licensee MDPI, Basel, Switzerland. This article is an open access article distributed under the terms and conditions of the Creative Commons Attribution (CC BY) license (<https://creativecommons.org/licenses/by/4.0/>).

## 1. Introduction

Diesel engines have durability and environmental friendliness [1,2]. However, the soot particles discharged by diesel engines are the main cause of hazy weather and lead to severe environmental pollution. Soot particles can also adsorb other harmful substances and cause serious harm to humans [3]. Therefore, reducing or eliminating the soot particles discharged by diesel engines is crucial. The use of diesel particulate filters (DPFs) for aftertreatment technology is an effective method for controlling soot emission, which requires the development of highly active catalysts to ensure the periodic regeneration of the DPF [4,5].

Noble metal catalysts display high activity for soot combustion and are extensively used as three-way catalysts [6,7]. However, the expensive price of noble metal catalysts has limited their broader application [8,9]. Researchers have developed various catalysts for catalytic soot combustion. Alkali metal catalysts feature a high surface fluidity, however, the low melting and boiling points of alkali metals can lead to their loss at high temperatures [10]. Transition metal catalysts have lower prices, but their catalytic activity is not ideal and is also prone to poisoning [11]. Rare-earth metal catalysts have a good poisoning resistance, high melting and boiling points, and a high economic value. CeO<sub>2</sub> has shown an excellent catalytic performance because it has the capacity for converting between the +3 and +4 valence of cerium, which can produce more active oxygen species [12–15]. Huang et al. [16] prepared nano-CeO<sub>2</sub> catalysts via a precipitation method and evaluated their catalytic activity. The ignition temperature of the soot oxidation reaction was 348 °C. Pure CeO<sub>2</sub> exhibits high activity in soot combustion, but its thermal stability is poor. High-temperature calcination will cause the sintering of CeO<sub>2</sub>, reducing its catalytic activity. In this regard, introducing other metals into CeO<sub>2</sub> can improve this shortcoming [17–20].

Manganese has an outstanding redox ability, and its incorporation into CeO<sub>2</sub> can enhance the activity of catalysts [21–23]. Lin et al. [24] synthesized a MnO<sub>x</sub>–CeO<sub>2</sub> catalyst and concluded that entering manganese into CeO<sub>2</sub> is beneficial for forming oxygen vacancies. Wang et al. [25] hydrothermally synthesized a Mn<sub>x</sub>Ce<sub>1–x</sub>O<sub>2</sub> solid solution catalyst, which had a unique mesoporous nanosheet structure and abundant active oxygen species.

The contact of the catalyst and soot particle also affects its activity [26]. Zhang et al. [27] synthesized CeO<sub>2</sub> with nanorod, nanoparticle, and nanosheet morphologies via hydrothermal and solvothermal methods. Among them, the CeO<sub>2</sub> nanorods exhibited the lowest peak temperatures of soot combustion, at approximately 368 °C, under tight contact modes. Therefore, designing and synthesizing cerium-based oxide catalysts with preferred morphologies could improve their contact efficiency with soot particles, thereby reducing the soot combustion temperature and improving the catalytic performance [28–30].

In this work, we first synthesized a range of MnO<sub>x</sub>/CeO<sub>2</sub> nanosphere catalysts, analyzed the physical and chemical properties of the MnO<sub>x</sub>/CeO<sub>2</sub> nanosphere catalysts using various characterization techniques, and ultimately evaluated their activity for soot combustion.

## 2. Experimental Section

### 2.1. Catalyst Preparation

#### 2.1.1. Preparation of CeO<sub>2</sub> Nanospheres

Some improvements were made to the previously reported preparation methods of CeO<sub>2</sub> nanospheres [31]. Ce(NO<sub>3</sub>)<sub>3</sub>·6H<sub>2</sub>O (2.5 g) and polyethylene pyrrolidone (1 g, K90) were added into a mixture solution of deionized water (10 mL) and ethylene glycol (70 mL), and the mixture was stirred until the solution became transparent. The solution was transferred to a 150 mL stainless steel autoclave and reacted at 160 °C for 24 h. After cooling, the product was centrifugally washed multiple times using anhydrous ethanol and deionized water until the upper solution was colorless. The products were dried at 80 °C for 12 h and then calcined at 500 °C for 3 h (2 °C/min).

#### 2.1.2. Preparation of MnO<sub>x</sub>/CeO<sub>2</sub> Nanosphere Catalysts

First, the CeO<sub>2</sub> nanospheres (0.6 g) and a certain amount of Mn(NO<sub>3</sub>)<sub>2</sub> (50% solution) in Mn/Ce molar ratios of 1:16, 1:8, 1:4, 1:2, and 1:1 were added to deionized water (55 mL) and ultrasonically treated for 15 min. Next, 1 mol/L of NaOH solution was dropwise added into the solution to adjust it to pH 10 under continuous stirring. The solution was transferred to a 100 mL stainless steel autoclave and reacted at 120 °C for 24 h after stirring for two hours. After cooling, the product was centrifugally washed multiple times. The products were dried at 80 °C for 12 h and calcined at 500 °C for 3 h (2 °C/min). The prepared MnO<sub>x</sub>/CeO<sub>2</sub> nanosphere catalysts are referred to as MnCe-1:16, MnCe-1:8, MnCe-1:4, MnCe-1:2, and MnCe-1:1 based on their Mn/Ce ratio. As shown in Table 1, we selected the MnCe-1:8, MnCe-1:4, and MnCe-1:1 catalysts to determine the contents of cerium and manganese elements in the catalysts via ICP measurement. From the ICP results, it can be observed that the actual content of Mn element in the catalyst increased with increasing the Mn/Ce molar ratios, while the actual content of Ce element showed a downward trend. However, the content of Mn element did not match the actual feeding ratio, which may have been due to the fact that MnO<sub>x</sub> did not grow on the CeO<sub>2</sub> support during the hydrothermal process and was lost after centrifugal washing.

**Table 1.** The actual contents of cerium and manganese elements in the catalysts.

Catalysts	Ce	Mn
MnCe-1:8	76.0%	3.8%
MnCe-1:4	72.1%	6.8%
MnCe-1:1	53.5%	21.4%

### 2.1.3. Preparation of MnO<sub>x</sub> Catalysts

The MnO<sub>x</sub> catalyst was prepared via the following steps. Firstly, Mn(NO<sub>3</sub>)<sub>2</sub> (50% solution, 2.06 g) was added into 55 mL of deionized water. The pH of the solution was adjusted to 10 by the dropwise addition of ammonia aqueous (25% solution) under constant stirring. The solution was transferred to a 100 mL stainless steel autoclave and reacted at 120 °C for 24 h after stirring for two hours, which was then allowed to cool. The product was washed multiple times via centrifugation. Finally, the products were dried at 80 °C for 12 h and calcined at 500 °C for 3 h (2 °C/min).

### 2.2. Catalyst Characterization

X-ray diffraction (XRD) with a scanning range of 10–90° and a speed of 10°/min using Cu K $\alpha$  radiation was conducted on the Rigaku Ultima IV X-ray diffractometer.

N<sub>2</sub> adsorption/desorption was conducted on the Micromeritics Tristar II 3020 specific surface analyzer. Before conducting the analysis, the catalyst was pretreated under vacuum and 300 °C conditions for 3 h.

Scanning electron microscopy (SEM) images were obtained using the Hitachi SU8010 system, and to improve the quality of the SEM images, 10 nm gold nanoparticles were coated on the catalyst surface prior to imaging. Transmission Electron Microscopy (TEM) was observed on a Thermo Scientific Talos F200x transmission electron microscope and an EDX analysis was performed on the same device. Before conducting the transmission electron microscopy observation, the catalyst was first ultrasonically treated in anhydrous ethanol for 15 min, and then the upper clear liquid was dropped onto a copper grid.

A H<sub>2</sub> temperature-programmed reduction (H<sub>2</sub>-TPR) was obtained using the Micromeritics AutoChem II 2920 chemical adsorption system. First, 100 mg of catalyst was pretreated under conditions of N<sub>2</sub> gas and 300 °C, and then cooled. The gas was replaced with a hydrogen/argon mixture, and the temperature was raised to 850 °C (10 °C/min). The hydrogen consumption was detected using a thermal conductivity detector. O<sub>2</sub> temperature-programmed desorption (O<sub>2</sub>-TPD) was performed on the same instrument, which differed from the H<sub>2</sub>-TPR method in that the catalyst was pretreated in O<sub>2</sub> gas, and then the gas was changed to He. The amount of O<sub>2</sub> desorption was detected using the same thermal conductivity detector.

X-ray photoelectron spectroscopy (XPS) was performed on a Thermo ESCALAB 250Xi instrument. The carbon 1s peak was set to 284.8 eV.

Soot-TPR was conducted in 50 mL/min Ar gas. In total, 100 mg of catalyst was mixed with 10 mg of soot to achieve a loose-contact mode. The mixture was pretreated at 200 °C and under Ar gas conditions for 30 min, and then heated from 200 °C to 800 °C (4 °C/min). The outlet gas composition was detected using the Agilent 7890B gas chromatograph.

In situ DRIFTS spectra was obtained using a Vertex 80v spectrometer (Bruker) FT-IR spectrometer. Before starting adsorption, the catalyst was pretreated in Ar gas at 500 °C for 0.5 h. During the cooling process, the background spectrum was scanned every 50 °C. Then, the gas was changed to NH<sub>3</sub> after adsorbing and saturating, then changed to Ar gas, and blown for 30 min. Finally, it was heated up to 500 °C and the infrared spectrum was recorded every 50 °C.

NO temperature-programmed oxidation (NO-TPO) was conducted on an optical flue gas analyzer FGA10. In total, 100 mg of catalyst was pretreated in Ar gas at 200 °C for 30 min, then heated from 100 °C to 500 °C (2 °C/min) under conditions of 10% O<sub>2</sub>, 800 ppm NO<sub>x</sub>, and Ar balance (100 mL/min).

### 2.3. Catalytic Activity Measurements

The catalytic performance of the catalysts was measured using the TPO method. Simulated soot was purchased from Frankfurt Degussa, Germany, and consisted of Printx-U particles with a diameter of 25 nm. Its elemental composition was 92.0% C, 3.5% O, 3.5% other elements, 0.7% H, 0.2% S, and 0.1% N. A total of 100 mg of catalyst with 10 mg of soot was mixed using a spatula to achieve a loose contact mode (or ground in

an agate mortar for 10 min to achieve a tight contact mode). Under a total 50 mL/min flow of 10% O<sub>2</sub>, 2000 ppm NO, and Ar balance, the mixture was heated from 100 °C to 650 °C on a fixed-bed tubular quartz reactor ( $\Phi = 8$  mm, 2 °C/min). The composition of the outlet gas was analyzed using the Agilent 7890B gas chromatograph. At 380 °C, the Ni catalyst completely converted CO and CO<sub>2</sub> into CH<sub>4</sub>. The temperatures T<sub>10</sub>, T<sub>50</sub>, and T<sub>90</sub>, corresponding to the soot conversion rates of 10%, 50%, and 90%, were used to evaluate the activity of the catalyst. The calculation formula for CO<sub>2</sub> selectivity ( $S_{CO_2}$ ) is  $S_{CO_2} = C_{CO_2} / (C_{CO} + C_{CO_2})$ .  $C_{CO_2}$  and  $C_{CO}$  represent the outlet concentrations of CO<sub>2</sub> and CO, respectively, and the  $S_{CO_2}^{max}$  is the CO<sub>2</sub> selectivity when the combustion rate of soot was the fastest.

### 3. Result and Discussion

#### 3.1. Structural Features of the Synthesized Catalysts

##### 3.1.1. XRD Analysis

Figure 1 presents the XRD results. In Figure 1(a–f), four distinct peaks are located at  $2\theta$  values of 28.5° (111), 33.1° (200), 47.5° (220), and 56.3° (311), corresponding to the characteristic peaks of CeO<sub>2</sub> (indicated with “★” in Figure 1, JCPDS Card No. 43-1002) [32,33]. The positions of the peaks for the MnO<sub>x</sub>/CeO<sub>2</sub> nanosphere catalysts were consistent with those for the CeO<sub>2</sub> support, demonstrating that the loading of MnO<sub>x</sub> would not affect the structure of CeO<sub>2</sub>. No diffraction peaks other than CeO<sub>2</sub> are observed in Figure 1(a–f), which may be because of the high dispersion of MnO<sub>x</sub>. In addition, as seen in Figure 1(g), the XRD results exhibited that the prepared MnO<sub>x</sub> catalyst showed distinct peaks located at  $2\theta$  values of 23.1° (211), 32.9° (222), 38.2° (400), and 55.2° (044), corresponding to the characteristic peaks of bixbyite Mn<sub>2</sub>O<sub>3</sub> (indicated with “◆” in Figure 1, JCPDS Card No. 41-1442) [34].

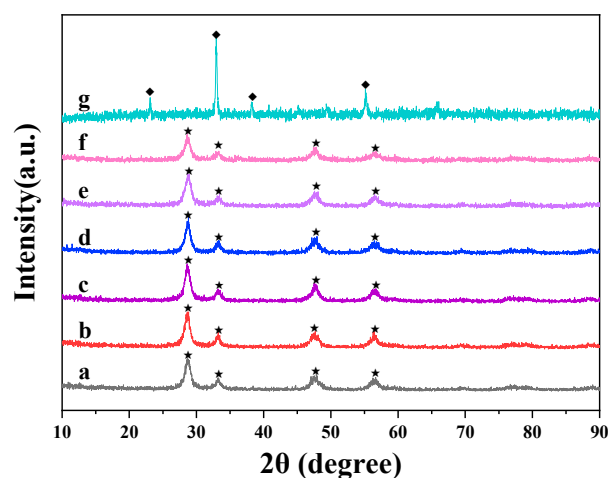


**Figure 1.** XRD results (a: CeO<sub>2</sub>; b: MnCe-1:16; c: MnCe-1:8; d: MnCe-1:4; e: MnCe-1:2; f: MnCe-1:1; and g: Mn<sub>2</sub>O<sub>3</sub>).

##### 3.1.2. N<sub>2</sub> Physisorption Analysis

Figure 2 shows the N<sub>2</sub> physisorption results of the catalysts. According to the definition of IUPAC, the catalysts showed typical type IV adsorption/desorption isotherms [35]. In Figure 2, H<sub>2</sub> hysteresis loops appear within the range of 0.9–1.0 relative pressure ( $P/P_0$ ), and the catalysts have a mesoporous structure in the range of 2–20 nm. From Figure 2B(a–f), it can be observed that the original CeO<sub>2</sub> nanospheres had a rich pore structure with pore sizes of 20–60 nm. However, this pore structure disappeared with increasing manganese loading, which can be ascribed to the filling of the pores by the loaded manganese species. Table 2 shows a decreasing trend in the specific surface area of the catalyst, which may be relevant to the MnO<sub>x</sub> species filling the stacking pores between the nanospheres. The pore

volume remained within the range of 0.067–0.119 cm<sup>3</sup>/g for all of the catalysts, while the pore size ranged from 4.7 to 7.2 nm.

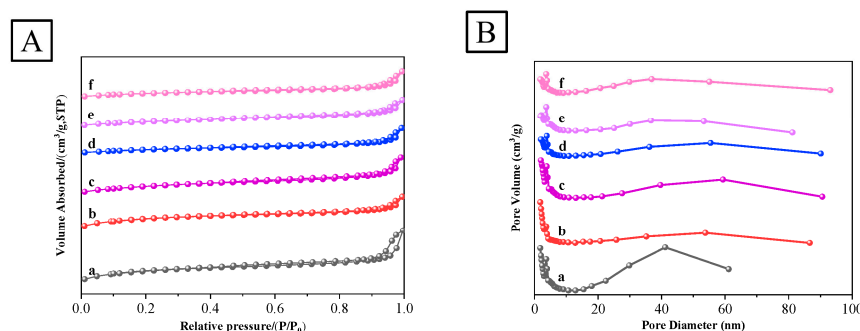


**Figure 2.** Nitrogen adsorption–desorption isotherms (A) and pore size distributions (B) of prepared catalysts (a: CeO<sub>2</sub>; b: MnCe-1:16; c: MnCe-1:8; d: MnCe-1:4; e: MnCe-1:2; and f: MnCe-1:1).

**Table 2.** Textural properties of prepared catalysts.

Catalysts	Surface Area (m <sup>2</sup> /g) <sup>a</sup>	Total Pore Volume (cm <sup>3</sup> /g) <sup>b</sup>	Pore Size (nm) <sup>c</sup>
CeO <sub>2</sub>	110.9	0.119	5.9
MnCe-1:16	95.5	0.083	4.7
MnCe-1:8	70.7	0.103	5.6
MnCe-1:4	38.4	0.070	6.9
MnCe-1:2	46.9	0.074	5.9
MnCe-1:1	43.2	0.067	7.2

<sup>a</sup> Calculated by BET method; <sup>b</sup> Calculated by BJH desorption cumulative volume of pores between 1.7 nm and 300 nm diameter; and <sup>c</sup> Calculated by BJH desorption average pore diameter.

### 3.1.3. Morphological Characterization of the Prepared Catalysts

Figure 3 shows the morphology of the prepared catalysts. The original CeO<sub>2</sub> nanospheres exhibited a uniformly distributed nano-spherical structure (Figure 3A). As shown in Figure 3B–D, after the hydrothermal growth of the manganese species, when the Mn/Ce ratios were 1:16, 1:8, and 1:4, the catalyst morphology did not undergo significant changes. However, as shown in Figure 3E,F, further increasing the manganese loading to Mn/Ce ratios of 1:2 and 1:1 led to the destruction of the nano-spherical structure and adhesion between the MnO<sub>x</sub>/CeO<sub>2</sub> nanospheres. The TEM image of the MnCe-1:4 catalyst is shown in Figure 3G, and the catalyst exhibits nano-spherical morphology. Based on the HAADF-STEM image (Figure 3H), elemental mapping images (Figure 3I–K), and the EDS spectrum (Figure 3L), the MnO<sub>x</sub> species had a good dispersibility in the MnCe-1:4 catalyst, with a Ce element content of 18.59% and a Mn element content of 6.07% (Mn:Ce = 1:3.06), which were approximated with the surface content of elements obtained from XPS (Mn:Ce = 1:3.38).

### 3.1.4. H<sub>2</sub>-TPR Analysis

The reduction performance of the MnO<sub>x</sub>/CeO<sub>2</sub> nanosphere catalysts was investigated using H<sub>2</sub>-TPR. In Figure 4(a), the peak of the CeO<sub>2</sub> nanospheres at 483 °C corresponds to the reduction in surface CeO<sub>2</sub> to Ce<sub>2</sub>O<sub>3</sub>. The peak of 600–800 °C corresponds to the reduction in bulk-phase CeO<sub>2</sub>. After the manganese species loading, the positions and types of reduction peaks changed. In Figure 4(b–f), the three reduction peaks from low to high temperatures below 500 °C can be attributed to the reduction in the surface-adsorbed oxygen, Mn<sup>4+</sup> to Mn<sup>3+</sup>, and Mn<sup>3+</sup> to Mn<sup>2+</sup> [34,36]. The reduction peak located above 600 °C belongs to the reduction in CeO<sub>2</sub> [37]. In addition, a lower peak temperature indicated a more facile reduction and a larger peak area reflected a greater hydrogen consumption. In Figure 4, the reduction peaks increase in area and shift toward lower temperatures with increasing manganese loading.

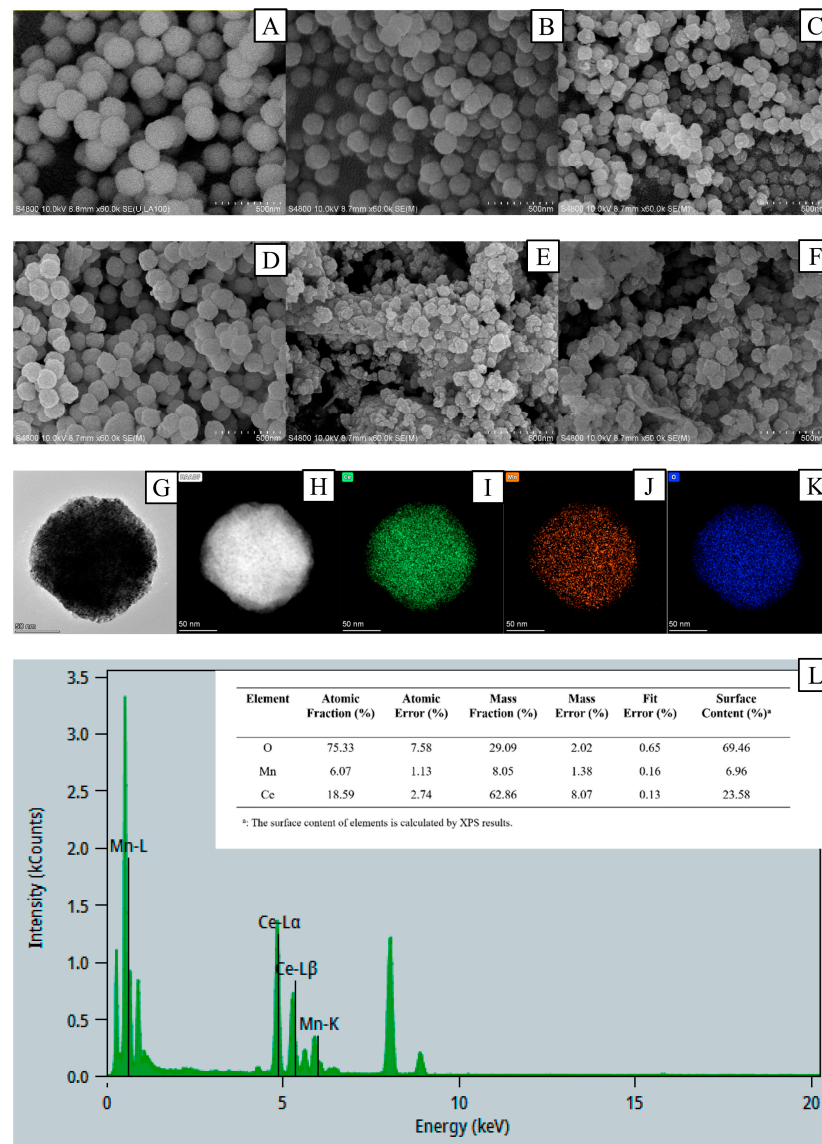


**Figure 3.** SEM (A–F) images of prepared catalysts ((A): CeO<sub>2</sub>; (B): MnCe-1:16; (C): MnCe-1:8; (D): MnCe-1:4; (E): MnCe-1:2; and (F): MnCe-1:1), TEM (G), HAADF-STEM (H), elemental mapping images (I–K), and EDS spectrum (L) of MnCe-1:4 catalyst.

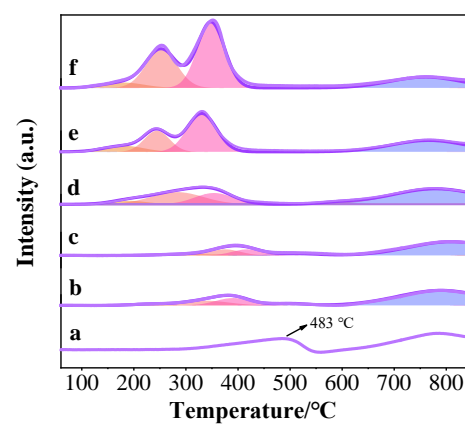


**Figure 4.** H<sub>2</sub>-TPR results (a: CeO<sub>2</sub>; b: MnCe-1:16; c: MnCe-1:8; d: MnCe-1:4; e: MnCe-1:2; and f: MnCe-1:1).

### 3.1.5. O<sub>2</sub>-TPD Analysis

Figure 5 shows the O<sub>2</sub>-TPD results. The desorption peak of the oxygen physisorbed on the catalyst surface (O<sub>2</sub> or O<sub>sur</sub>, labeled α) is within the range of 50–250 °C. The chemically adsorbed (O<sub>2</sub><sup>-</sup>/O<sup>-</sup>, named as β) desorption peak ranges from 250 to 450 °C. Finally, the desorption peak in the range of 450–850 °C corresponds to the lattice oxygen (O<sup>2-</sup>, named as γ) [38–40]. As can be observed from Figure 5, the MnCe-1:4 catalyst resulted in the largest peak area for the chemically adsorbed oxygen species in the β region; therefore, it had the most active oxygen species.

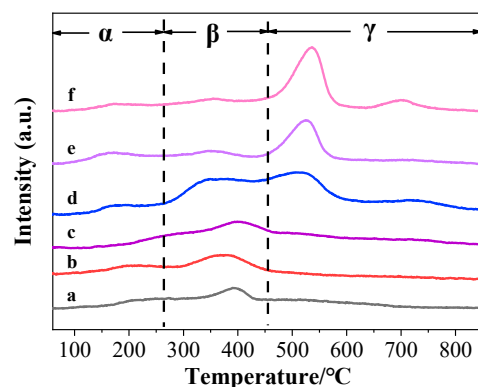


**Figure 5.** O<sub>2</sub>-TPD results (a: CeO<sub>2</sub>; b: MnCe-1:16; c: MnCe-1:8; d: MnCe-1:4; e: MnCe-1:2; and f: MnCe-1:1).

### 3.1.6. XPS Analysis

As shown in Figure 6 and Table 3, the CeO<sub>2</sub>, MnCe-1:16, MnCe-1:4, and MnCe-1:1 catalysts were selected as representative catalysts for the XPS characterization. Figure 6A shows the cerium 3d spectrum, which could be fitted by eight peaks based on four pairs of spin-orbit doublets [41–43]. When the manganese species were loaded onto a CeO<sub>2</sub> support, Ce<sup>4+</sup> would transform into Ce<sup>3+</sup> and oxygen vacancies were generated. Table 3 shows the calculated ratios of the Ce<sup>3+</sup> peak area to the total cerium peak area, which were used to estimate the relative Ce<sup>3+</sup> contents on the catalyst surfaces. It can be concluded that, as the manganese content increased, the Ce<sup>3+</sup> content first increased and then decreased. The MnCe-1:4 catalyst had the highest Ce<sup>3+</sup> content at 18.59%, which meant it contained the most surface oxygen vacancies.

Figure 6B shows the manganese 2p spectrum. Due to the difficulty in distinguishing the valence state of the manganese solely based on the Mn 2p spectrum, the manganese 3s spectra were also measured to confirm the valence states. The correlation between ΔE and the average valence state of the manganese can be expressed as follows: average valence state = 8.95 – 1.13 × ΔE [44,45]. From Figure 6C, it can be seen that the ΔE values for the MnCe-1:4 and MnCe-1:1 catalysts were 5.43 and 5.10 eV, indicating average valence states of 2.81 and 3.19, respectively. Previous studies have shown that high-valent Mn<sup>4+</sup> cations in oxides are often reduced to Mn<sup>3+</sup> with the formation of oxygen vacancies (V<sub>o</sub>), as follows: 2Mn<sup>4+</sup> + O<sup>2-</sup> → 2Mn<sup>3+</sup> + V<sub>o</sub> + 0.5O<sub>2(g)</sub> [46,47]. From Table 3, it can be seen that the MnCe-1:4 catalyst had the highest Mn<sup>3+</sup> content among the catalysts, indicating that it had more oxygen vacancies.

Figure 6D shows the oxygen 1s spectrum, from which three types of oxygen species can be observed. The O-I species with binding energies of 531.94–532.70 eV corresponds to the surface-adsorbed oxygen (O<sub>sur</sub>), the O-II species with binding energies of 530.84–531.57 eV corresponds to the chemically adsorbed oxygen (O<sub>ads</sub>), and the O-III species with binding energies of 529.10–530.0 eV corresponds to the lattice oxygen (O<sub>latt</sub>) [48]. Combined with the O<sub>2</sub>-TPD results, these three kinds of oxygen species are consistent with the XPS results. However, the contents of the three oxygen species obtained by O<sub>2</sub>-TPD are different from the XPS results. The reason for this phenomenon is as follows: XPS can directly detect the proportions of the three oxygen species in the catalyst, while the O<sub>2</sub>-TPD detects the

released oxygen species from the catalyst. Similar to the O<sub>2</sub>-TPD results, with the increase in manganese loading, the proportion of O-II species first increased and then decreased. The MnCe-1:4 catalyst had the most O-II species.

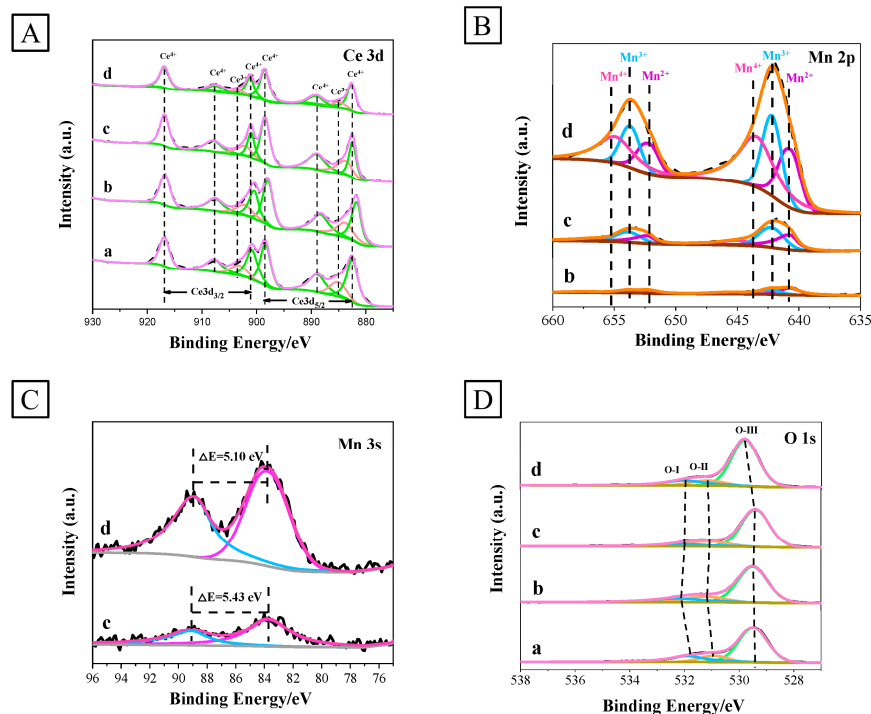


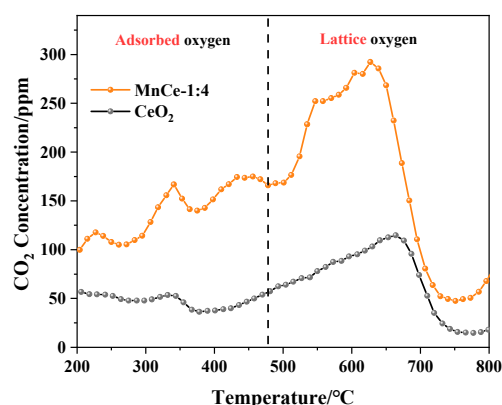
Figure 6. XPS spectra (A: CeO<sub>2</sub>; B: MnCe-1:16; C: MnCe-1:4; and D: MnCe-1:1).

Table 3. Composition and oxidation state of manganese, cerium, and oxygen on the surface of prepared catalyst.

Sample	Molar Fraction							
	Manganese			Cerium		Oxygen		
	Mn <sup>4+</sup>	Mn <sup>3+</sup>	Mn <sup>2+</sup>	Ce <sup>4+</sup>	Ce <sup>3+</sup>	O <sub>latt</sub>	O <sub>ads</sub>	O <sub>sur</sub>
CeO <sub>2</sub>				85.11%	14.89%	68.16%	11.71%	20.13%
MnCe-1:16	17.34%	26.21%	56.45%	81.94%	18.06%	69.94%	14.15%	15.91%
MnCe-1:4	16.78%	47.04%	36.18%	81.41%	18.59%	74.04%	14.70%	11.26%
MnCe-1:1	43.95%	30.56%	25.48%	92.19%	7.81%	74.07%	9.97%	15.96%

### 3.1.7. Soot-TPR Analysis

Soot-TPR can reflect the situation of oxygen defect sites in the catalyst [46]. Therefore, we conducted Soot-TPR measurements on the CeO<sub>2</sub> and MnCe-1:4 catalysts. As shown in Figure 7, the peaks at 200–480 °C belong to the surface-adsorbed oxygen, and the peaks at 480–800 °C belong to the lattice oxygen. Compared to the CeO<sub>2</sub> catalyst, the amount of CO<sub>2</sub> generated by the MnCe-1:4 catalyst significantly increased, indicating that the catalyst had more oxygen defect sites [49,50]. At the same time, the MnCe-1:4 catalyst had a lower temperature for the desorption of lattice oxygen, so the loading of Mn species could generate more active oxygen species and promote their migration, which suggests that the contents of oxygen vacancies were abundant when Mn species were loaded on the CeO<sub>2</sub>. Meanwhile, the variation tendency of oxygen vacancies is also consistent with the catalyst activities of catalysts.



**Figure 7.** Soot-TPR curves of CeO<sub>2</sub> and MnCe-1:4 catalysts.

### 3.1.8. NO-TPO Analysis

The conversion ability of NO<sub>x</sub> can affect the catalytic activities of catalysts for soot combustion. Therefore, we tested the NO<sub>2</sub> concentration (Figure 8A) and NO concentration (Figure 8B) of the CeO<sub>2</sub> and MnCe-1:4 catalysts under different temperatures. From Figure 8A, it can be seen that the NO<sub>2</sub> concentration of the CeO<sub>2</sub> and MnCe-1:4 catalysts first increased and then decreased. Among them, the CeO<sub>2</sub> catalyst reached its maximum concentration of NO<sub>2</sub> at about 403 °C. Compared to CeO<sub>2</sub>, the MnCe-1:4 catalyst generated a higher NO<sub>2</sub> content and lower temperature (about 340 °C) for the maximum NO<sub>2</sub> concentration, while the trend of NO concentration in Figure 8B is opposite to that of NO<sub>2</sub>. The results suggested that the MnO<sub>x</sub> species loading on CeO<sub>2</sub> could improve the NO oxidation capacity.

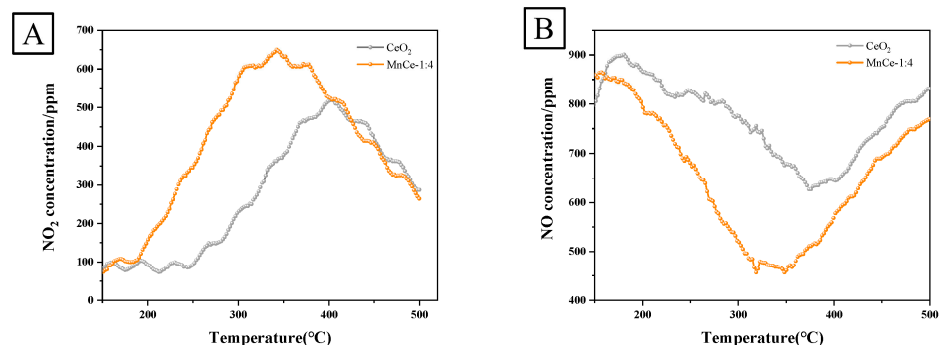


**Figure 8.** NO<sub>2</sub> concentration (A) and NO concentration profiles (B) over CeO<sub>2</sub> and MnCe-1:4 catalysts.

### 3.1.9. In situ DRIFTS Analysis

The acid sites on the catalyst surface were investigated using NH<sub>3</sub> adsorption/desorption in situ infrared spectroscopy. Figure 9A,B show the IR spectra of the CeO<sub>2</sub> and MnCe-1:4 catalysts under the temperature range of 100–500 °C, respectively. As shown in Figure 9A, the surface components of the CeO<sub>2</sub> catalyst were mainly Lewis acid-coordinated ammonia (1179 cm<sup>-1</sup>) and Brønsted acid-coordinated NH<sub>4</sub><sup>+</sup> (1448 cm<sup>-1</sup>) [51,52]. When the temperature rose to 400 °C, NH<sub>3</sub> desorption occurred on the surface of CeO<sub>2</sub>, and the Lewis acid sites gradually decreased. After loading manganese species on the CeO<sub>2</sub> support, the types of acid sites did not change, which were Lewis acid-coordinated ammonia (1227 cm<sup>-1</sup>) and Brønsted acid-coordinated NH<sub>4</sub><sup>+</sup> (1448 cm<sup>-1</sup>) (Figure 9B) [53]. From Figure 9, it can be concluded that, when Mn species were loaded onto the CeO<sub>2</sub> support, the Lewis acid sites changed and the peak intensity increased due to the simultaneous adsorption of NH<sub>3</sub> by Mn. Based on the above discussion, the improvement in catalytic activity may have been related to the increase in the number of acid sites.

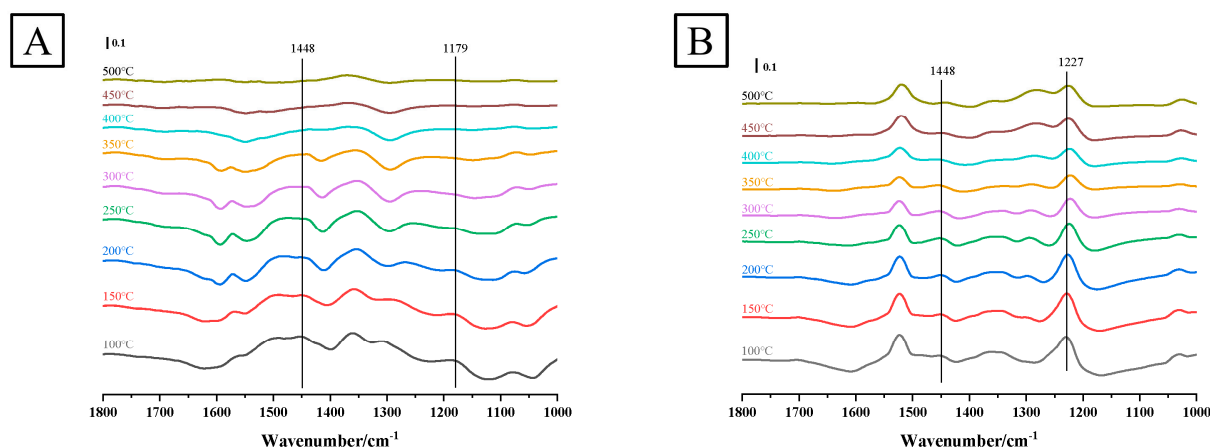


**Figure 9.** In situ DRIFTS spectra of  $\text{CeO}_2$  (A) and  $\text{MnCe-1:4}$  catalysts (B).

### 3.2. Catalytic Performance in Soot Combustion

Table 4 shows the activities of the prepared catalysts and pure soot under loose contact mode. The catalytic activity of the pure  $\text{CeO}_2$  support was weak, but the catalytic activity was significantly improved after loading the manganese species; among them, the  $\text{MnCe-1:4}$  catalyst had the highest activity, with  $T_{10}$ ,  $T_{50}$ , and  $T_{90}$  values of 289, 340, and 373 °C, respectively. Due to the small difference in catalytic performance between the catalysts with different Mn loadings, three repeated activity tests were conducted on the  $\text{MnCe-1:4}$  catalyst to test the repeatability and stability of the activity test method in this work. Table 5 shows the activity of the three repeated tests, and the relative errors ( $\delta$ ) of the repeated activity tests were calculated. As shown in Table 5, all the values of the relative errors were less than 2%. Therefore, it can be concluded that the activity test method had a high reliability. Therefore, the catalytic activity of the  $\text{MnO}_x/\text{CeO}_2$  catalysts was meaningful. We also tested the catalytic performance of the  $\text{MnCe-1:4}$  catalyst under tight contact mode. According to Table 4, the activity of the catalyst slightly increased. Therefore, the catalyst–soot contact mode had an impact on the catalyst activity. In addition, we tested the catalytic performance of the pure  $\text{Mn}_2\text{O}_3$  and mechanical mixing of the  $\text{Mn}_2\text{O}_3$  and  $\text{CeO}_2$  catalysts for soot combustion. As shown in Table 4, the catalytic activities of the pure  $\text{Mn}_2\text{O}_3$  and the mechanical mixing of the  $\text{CeO}_2$  and  $\text{Mn}_2\text{O}_3$  catalysts were lower than that of the  $\text{MnO}_x/\text{CeO}_2$  catalysts. Therefore, the interaction between Mn and Ce was one of the reasons for the excellent catalytic activity of the  $\text{MnO}_x/\text{CeO}_2$  catalysts. For further comparison, the catalytic performance of the  $\text{MnCe-1:4}$  catalyst was compared with that of other cerium-based oxide catalysts (Table 6). Compared to  $\text{CeO}_2$  nanocubes without other active components, the  $\text{MnCe-1:4}$  catalyst prepared in this study had lower  $T_{10}$ ,  $T_{50}$ , and  $T_{90}$  values, indicating that the interaction between Mn and Ce is beneficial for enhancing the catalytic combustion of soot. In addition, the combustion temperature values of the  $\text{MnCe-1:4}$  catalyst with a nano-sphere structure prepared in this study were lower than those of the  $\text{CeO}_2@\text{MnO}_2$  catalyst with a core–shell structure, the catalysts with three-dimensionally ordered macropores (3DOM), such as  $(\text{NiO-CeO}_2)\text{-3DOM}$ ,  $3\text{DOM Co}_3\text{O}_4\text{-CeO}_2$ , and  $3\text{DOM Mn}_{0.5}\text{Ce}_{0.5}\text{O}_8$ , and the  $\text{MnO}_x\text{-CeO}_2\text{-Al}_2\text{O}_3$  catalyst without a special morphology. This means that the nano-sphere structure of the  $\text{MnCe-1:4}$  catalyst was beneficial for improving the contact efficiency between the soot and the catalyst, and had a superior soot combustion activity. The  $\text{MnCe-1:4}$  catalyst prepared in this study had higher catalytic activity, indicating that the nano-spherical morphology of the catalyst, abundant active oxygen species, and the interaction between Mn and Ce species are beneficial for enhancing soot combustion.

**Table 4.** Catalytic performance of prepared catalysts for soot combustion.

Catalysts	T <sub>10</sub> /°C	T <sub>50</sub> /°C	T <sub>90</sub> /°C	S <sub>CO<sub>2</sub><sup>m</sup></sub> /%
Soot	461	552	594	38.5%
CeO <sub>2</sub>	318	363	402	96.5%
Mn <sub>2</sub> O <sub>3</sub>	294	357	395	99.6%
Mn <sub>2</sub> O <sub>3</sub> + CeO <sub>2</sub> (mechanical mixing)	294	350	384	99.5%
MnCe-1:16	294	350	384	99.5%
MnCe-1:8	292	344	375	99.3%
MnCe-1:4	289	340	373	99.3%
MnCe-1:4 (under tight contact mode)	278	327	353	99.6%
MnCe-1:2	286	347	382	99.5%
MnCe-1:1	286	346	383	99.5%

**Table 5.** The catalytic activity of the MnCe-1:4 catalyst was repeatedly tested for soot combustion three times in loose contact mode, and the relative error was calculated.

Catalysts <sup>a</sup>	T <sub>10</sub> /°C	δ <sup>b</sup>	T <sub>50</sub> /°C	δ	T <sub>90</sub> /°C	δ	S <sub>CO<sub>2</sub><sup>m</sup></sub> /%	δ
MnCe-1:4-1	291	0.69%	340	0%	379	1.6%	99.5%	0.20%
MnCe-1:4-2	292	1.04%	342	0.59%	374	0.27%	99.6%	0.30%
MnCe-1:4-3	290	0.35%	337	0.88%	373	0%	99.6%	0.30%

<sup>a</sup>: Three repeated activity tests were performed on MnCe-1:4 catalyst; <sup>b</sup>: Calculation formula for relative error:  $\delta = (x - \mu) / \mu \times 100\%$ ,  $x$  represents the T<sub>10</sub>/T<sub>50</sub>/T<sub>90</sub>/S<sub>CO<sub>2</sub><sup>m</sup></sub> of the catalysts for repeated activity testing, and  $\mu$  represents the value of T<sub>10</sub>/T<sub>50</sub>/T<sub>90</sub>/S<sub>CO<sub>2</sub><sup>m</sup></sub> corresponding to MnCe-1:4 catalyst.

**Table 6.** Catalytic activities of as-prepared catalysts and reported catalysts for soot combustion under loose contact conditions.

Catalysts	Reaction Conditions	Soot/ Catalysts	T <sub>10</sub> /T <sub>i</sub> (°C)	T <sub>50</sub> /T <sub>m</sub> (°C)	T <sub>90</sub> /T <sub>f</sub> (°C)	References
CeO <sub>2</sub> @MnO <sub>2</sub>	500 ppm NO + 5% O <sub>2</sub> + N <sub>2</sub> balance	1:9	312	373	423	[32]
(NiO-CeO <sub>2</sub> )-3DOM	500 ppm NO + 5% O <sub>2</sub> + N <sub>2</sub> balance	1:4		530		[54]
CeO <sub>2</sub> nanocube	10 vol.% O <sub>2</sub> + N <sub>2</sub> balance	1:10		459	554	[55]
3DOM Co <sub>3</sub> O <sub>4</sub> -CeO <sub>2</sub>	0.25% NO + 5% O <sub>2</sub> + N <sub>2</sub> balance	1:10		406		[56]
MnO <sub>x</sub> -CeO <sub>2</sub> -Al <sub>2</sub> O <sub>3</sub>	1000 ppm NO + 10% O <sub>2</sub> + N <sub>2</sub> balance	1:10		455		[57]
3DOM Mn <sub>0.5</sub> Ce <sub>0.5</sub> O <sub>δ</sub>	0.2% NO + 10% O <sub>2</sub> + Ar balance	1:10	297	358	396	[58]
MnCe-1:4	2000 ppm NO + 10% O <sub>2</sub> + Ar balance	1:10	289	340	373	This work

#### 4. Conclusions

A series of manganese-loaded CeO<sub>2</sub> nanosphere catalysts were synthesized via a simple two-step hydrothermal method, and the prepared MnO<sub>x</sub>/CeO<sub>2</sub> catalysts exhibited excellent catalytic activity for soot combustion. The characterization results confirmed that the catalysts possessed a nano-spherical structure and revealed that the manganese loading affected the specific surface area and improved their O<sub>2</sub> adsorption and activation ability. Among the prepared catalysts, the MnCe-1:4 catalyst had the optimal catalytic performance, with T<sub>10</sub>, T<sub>50</sub>, and T<sub>90</sub> values of 289, 340, and 373 °C, respectively, and a CO<sub>2</sub> selectivity of 99.3%.

**Author Contributions:** Conceptualization, S.G. and X.Y.; methodology, S.G.; software, S.Z. and C.Z.; validation, D.Y., S.Z., C.Z. and L.W.; formal analysis, X.F.; investigation, S.G., D.Y. and S.Z.; resources, X.Y.; data curation, S.G.; Writing—Original draft preparation, S.G.; Writing—Review and editing, X.Y.; visualization, Z.Z.; supervision, X.Y.; project administration, Z.Z.; funding acquisition, X.F. All authors have read and agreed to the published version of the manuscript.

**Funding:** This research was funded by National Key R&D Program of China (2022YFB3506200, 2022YFB3504100); National Natural Science Foundation of China (22372107, 22072095, U1908204); Excellent Youth Science Foundation of Liaoning Province (2022-YQ-20); Shenyang Science and Technology Planning Project (22-322-3-28); University Joint Education Project for China-Central and Eastern European Countries (2021097); Major/Key Project of Graduate Education and Teaching Reform of Shenyang Normal University (YJSJG120210008/YJSJG220210022).

**Data Availability Statement:** All the data during the study appeared in the submitted article.

**Acknowledgments:** The instruments and equipment used in this work are supported by Major Platform for Science and Technology of the Universities in Liaoning Province: The Engineering Technology Research Center of Catalysis for Energy and Environment and The Belt and Road International Joint Research Center of Catalysis for Energy and Environment.

**Conflicts of Interest:** The authors declare no conflict of interest.

## References

1. Yu, X.; Wang, L.; Zhao, Z.; Fan, X.; Chen, M.; Wei, Y.; Liu, J. 3DOM SiO<sub>2</sub>-Supported Different Alkali Metals-Modified MnO<sub>x</sub> Catalysts: Preparation and Catalytic Performance for Soot combustion. *ChemistrySelect* **2017**, *2*, 10176–10185. [\[CrossRef\]](#)
2. Frank, B.; Schuster, M.E.; Schlögl, R.; Su, D.S. Emission of Highly Activated Soot Particulate—The Other Side of the Coin with Modern Diesel Engines. *Angew. Chem. Int. Ed.* **2013**, *52*, 2673–2677. [\[CrossRef\]](#) [\[PubMed\]](#)
3. Shao, J.; Lan, X.; Zhang, C.; Cao, C.; Yu, Y. Recent advances in soot combustion catalysts with designed micro-structures. *Chin. Chem. Lett.* **2022**, *33*, 1763–1771. [\[CrossRef\]](#)
4. Liu, S.; Wu, X.; Weng, D.; Ran, R. Ceria-based catalysts for soot oxidation: A review. *J. Rare Earths* **2015**, *33*, 567–590. [\[CrossRef\]](#)
5. Yeste, M.P.; Cauqui, M.Á.; Giménez-Mañogil, J.; Martínez-Munuera, J.C.; Muñoz, M.Á.; García-García, A. Catalytic activity of Cu and Co supported on ceria-yttria-zirconia oxides for the diesel soot combustion reaction in the presence of NO<sub>x</sub>. *Chem. Eng. J.* **2020**, *380*, 122370. [\[CrossRef\]](#)
6. Bueno-López, A. Diesel soot combustion ceria catalysts. *Appl. Catal. B* **2014**, *146*, 1–11. [\[CrossRef\]](#)
7. Lan, L.; Chen, S.; Li, H.; Wang, J.; Li, D.; Chen, Y. Optimized synthesis of highly thermal stable CeO<sub>2</sub>-ZrO<sub>2</sub>/Al<sub>2</sub>O<sub>3</sub> composite for improved Pd-only three-way catalyst. *Mater. Des.* **2018**, *147*, 191–199. [\[CrossRef\]](#)
8. Wei, Y.; Zhao, Z.; Liu, J.; Xu, C.; Jiang, G.; Duan, A. Design and Synthesis of 3D Ordered Macroporous CeO<sub>2</sub>-Supported Pt@CeO<sub>2-δ</sub> Core-Shell Nanoparticle Materials for Enhanced Catalytic Activity of Soot Oxidation. *Small* **2013**, *9*, 3957–3963. [\[CrossRef\]](#)
9. Mukherjee, D.; Reddy, B.M. Noble metal-free CeO<sub>2</sub>-based mixed oxides for CO and soot oxidation. *Catal. Today* **2018**, *309*, 227–235. [\[CrossRef\]](#)
10. Liu, T.; Li, Q.; Xin, Y.; Zhang, Z.; Tang, X.; Zheng, L.; Gao, P.-X. Quasi free K cations confined in hollandite-type tunnels for catalytic solid (catalyst)-solid (reactant) oxidation reactions. *Appl. Catal. B* **2018**, *232*, 108–116. [\[CrossRef\]](#)
11. Neeft, J.P.A.; Makkee, M.; Moulijn, J.A. Metal oxides as catalysts for the oxidation of soot. *Chem. Eng. J. Biochem. Eng.* **1996**, *64*, 295–302. [\[CrossRef\]](#)
12. Zhang, L.; Zhao, X.; Yuan, Z.; Wu, M.; Zhou, H. Oxygen defect-stabilized heterogeneous single atom catalysts: Preparation, properties and catalytic application. *J. Mater. Chem. A* **2021**, *9*, 3855–3879. [\[CrossRef\]](#)
13. Ji, W.; Wang, N.; Li, Q.; Zhu, H.; Lin, K.; Deng, J.; Chen, J.; Zhang, H.; Xing, X. Oxygen vacancy distributions and electron localization in a CeO<sub>2</sub>(100) nanocube. *Inorg. Chem. Front.* **2022**, *9*, 275–283. [\[CrossRef\]](#)
14. Xu, B.; Xia, L.; Zhou, F.; Zhao, R.; Chen, H.; Wang, T.; Zhou, Q.; Liu, Q.; Cui, G.; Xiong, X.; et al. Enhancing Electrocatalytic N<sub>2</sub> Reduction to NH<sub>3</sub> by CeO<sub>2</sub> Nanorod with Oxygen Vacancies. *ACS Sustain. Chem. Eng.* **2019**, *7*, 2889–2893. [\[CrossRef\]](#)
15. Machida, M.; Ueno, M.; Omura, T.; Kurusu, S.; Hinokuma, S.; Nanba, T.; Shinozaki, O.; Furutani, H. CeO<sub>2</sub>-Grafted Mn-Fe Oxide Composites as Alternative Oxygen-Storage Materials for Three-Way Catalysts: Laboratory and Chassis Dynamometer Tests. *Ind. Eng. Chem. Res.* **2017**, *56*, 3184–3193. [\[CrossRef\]](#)
16. Huang, H.; Liu, J.; Sun, P.; Ye, S. Study on the simultaneous reduction of diesel engine soot and NO with nano-CeO<sub>2</sub> catalysts. *RSC Adv.* **2016**, *6*, 102028–102034. [\[CrossRef\]](#)
17. Lee, J.H.; Jo, D.Y.; Choung, J.W.; Kim, C.H.; Ham, H.C.; Lee, K.-Y. Roles of noble metals (M = Ag, Au, Pd, Pt and Rh) on CeO<sub>2</sub> in enhancing activity toward soot oxidation: Active oxygen species and DFT calculations. *J. Hazard. Mater.* **2021**, *403*, 124085. [\[CrossRef\]](#)
18. Wang, H.; Jin, B.; Wang, H.; Ma, N.; Liu, W.; Weng, D.; Wu, X.; Liu, S. Study of Ag promoted Fe<sub>2</sub>O<sub>3</sub>@CeO<sub>2</sub> as superior soot oxidation catalysts: The role of Fe<sub>2</sub>O<sub>3</sub> crystal plane and tandem oxygen delivery. *Appl. Catal. B* **2018**, *237*, 251–262. [\[CrossRef\]](#)
19. Shan, W.; Yang, L.; Ma, N.; Yang, J. Catalytic Activity and Stability of K/CeO<sub>2</sub> Catalysts for Diesel Soot Oxidation. *Chin. J. Catal.* **2012**, *33*, 970–976. [\[CrossRef\]](#)
20. Małecka, M.A.; Kepiński, L.; Miśta, W. Structure evolution of nanocrystalline CeO<sub>2</sub> and CeLnO<sub>x</sub> mixed oxides (Ln = Pr, Tb, Lu) in O<sub>2</sub> and H<sub>2</sub> atmosphere and their catalytic activity in soot combustion. *Appl. Catal. B* **2007**, *74*, 290–298. [\[CrossRef\]](#)
21. Cheng, L.; Men, Y.; Wang, J.; Wang, H.; An, W.; Wang, Y.; Duan, Z.; Liu, J. Crystal facet-dependent reactivity of α-Mn<sub>2</sub>O<sub>3</sub> microcrystalline catalyst for soot combustion. *Appl. Catal. B* **2017**, *204*, 374–384. [\[CrossRef\]](#)

22. Xu, H.; Yan, N.; Qu, Z.; Liu, W.; Mei, J.; Huang, W.; Zhao, S. Gaseous Heterogeneous Catalytic Reactions over Mn-Based Oxides for Environmental Applications: A Critical Review. *Environ. Sci. Technol.* **2017**, *51*, 8879–8892. [[CrossRef](#)] [[PubMed](#)]
23. Sun, M.; Yu, L.; Ye, F.; Diao, G.; Yu, Q.; Hao, Z.; Zheng, Y.; Yuan, L. Transition metal doped cryptomelane-type manganese oxide for low-temperature catalytic combustion of dimethyl ether. *Chem. Eng. J.* **2013**, *220*, 320–327. [[CrossRef](#)]
24. Lin, X.; Li, S.; He, H.; Wu, Z.; Wu, J.; Chen, L.; Ye, D.; Fu, M. Evolution of oxygen vacancies in MnO<sub>x</sub>-CeO<sub>2</sub> mixed oxides for soot oxidation. *Appl. Catal. B* **2018**, *223*, 91–102. [[CrossRef](#)]
25. Wang, J.; Yang, S.; Sun, H.; Qiu, J.; Men, Y. Highly improved soot combustion performance over synergetic Mn<sub>x</sub>Ce<sub>1-x</sub>O<sub>2</sub> solid solutions within mesoporous nanosheets. *J. Colloid Interface Sci.* **2020**, *577*, 355–367. [[CrossRef](#)] [[PubMed](#)]
26. Zhang, C.; Yu, D.; Peng, C.; Wang, L.; Yu, X.; Wei, Y.; Liu, J.; Zhao, Z. Research progress on preparation of 3DOM-based oxide catalysts and their catalytic performances for the combustion of diesel soot particles. *Appl. Catal. B* **2022**, *319*, 121946. [[CrossRef](#)]
27. Zhang, W.; Niu, X.; Chen, L.; Yuan, F.; Zhu, Y. Soot Combustion over Nanostructured Ceria with Different Morphologies. *Sci. Rep.* **2016**, *6*, 29062. [[CrossRef](#)]
28. Yang, Q.; Gu, F.; Tang, Y.; Zhang, H.; Liu, Q.; Zhong, Z.; Su, F. A Co<sub>3</sub>O<sub>4</sub>-CeO<sub>2</sub> functionalized SBA-15 monolith with a three-dimensional framework improves NO<sub>x</sub>-assisted soot combustion. *RSC Adv.* **2015**, *5*, 26815–26822. [[CrossRef](#)]
29. Zhang, G.; Zhao, Z.; Liu, J.; Jiang, G.; Duan, A.; Zheng, J.; Chen, S.; Zhou, R. Three dimensionally ordered macroporous Ce<sub>1-x</sub>Zr<sub>x</sub>O<sub>2</sub> solid solutions for diesel soot combustion. *ChemComm* **2010**, *46*, 457–459. [[CrossRef](#)]
30. Zhang, G.; Zhao, Z.; Xu, J.; Zheng, J.; Liu, J.; Jiang, G.; Duan, A.; He, H. Comparative study on the preparation, characterization and catalytic performances of 3DOM Ce-based materials for the combustion of diesel soot. *Appl. Catal. B* **2011**, *107*, 302–315. [[CrossRef](#)]
31. Su, Z.; Yang, W.; Wang, C.; Xiong, S.; Cao, X.; Peng, Y.; Si, W.; Weng, Y.; Xue, M.; Li, J. Roles of Oxygen Vacancies in the Bulk and Surface of CeO<sub>2</sub> for Toluene Catalytic Combustion. *Environ. Sci. Technol.* **2020**, *54*, 12684–12692. [[CrossRef](#)] [[PubMed](#)]
32. Feng, N.; Zhu, Z.; Zhao, P.; Wang, L.; Wan, H.; Guan, G. Facile fabrication of trepang-like CeO<sub>2</sub>@MnO<sub>2</sub> nanocomposite with high catalytic activity for soot removal. *Appl. Surf. Sci.* **2020**, *515*, 146013. [[CrossRef](#)]
33. Qi, G.; Yang, R.T.; Chang, R. MnO<sub>x</sub>-CeO<sub>2</sub> mixed oxides prepared by co-precipitation for selective catalytic reduction of NO with NH<sub>3</sub> at low temperatures. *Appl. Catal. B* **2004**, *51*, 93–106. [[CrossRef](#)]
34. Yu, X.; Wang, L.; Chen, M.; Fan, X.; Zhao, Z.; Cheng, K.; Chen, Y.; Sojka, Z.; Wei, Y.; Liu, J. Enhanced activity and sulfur resistance for soot combustion on three-dimensionally ordered macroporous-mesoporous Mn<sub>x</sub>Ce<sub>1-x</sub>O<sub>8</sub>/SiO<sub>2</sub> catalysts. *Appl. Catal. B* **2019**, *254*, 246–259. [[CrossRef](#)]
35. Sing, K.S.W. Reporting physisorption data for gas/solid systems with special reference to the determination of surface area and porosity (Recommendations 1984). *Pure Appl. Chem.* **1985**, *57*, 603–619. [[CrossRef](#)]
36. Yu, D.; Ren, Y.; Yu, X.; Fan, X.; Wang, L.; Wang, R.; Zhao, Z.; Cheng, K.; Chen, Y.; Sojka, Z.; et al. Facile synthesis of birnessite-type K<sub>2</sub>Mn<sub>4</sub>O<sub>8</sub> and cryptomelane-type K<sub>2-x</sub>Mn<sub>8</sub>O<sub>16</sub> catalysts and their excellent catalytic performance for soot combustion with high resistance to H<sub>2</sub>O and SO<sub>2</sub>. *Appl. Catal. B* **2021**, *285*, 119779. [[CrossRef](#)]
37. Chen, D.; He, D.; Lu, J.; Zhong, L.; Liu, F.; Liu, J.; Yu, J.; Wan, G.; He, S.; Luo, Y. Investigation of the role of surface lattice oxygen and bulk lattice oxygen migration of cerium-based oxygen carriers: XPS and designed H<sub>2</sub>-TPR characterization. *Appl. Catal. B* **2017**, *218*, 249–259. [[CrossRef](#)]
38. Yu, D.; Wang, L.; Zhang, C.; Peng, C.; Yu, X.; Fan, X.; Liu, B.; Li, K.; Li, Z.; Wei, Y.; et al. Alkali Metals and Cerium-Modified La-Co-Based Perovskite Catalysts: Facile Synthesis, Excellent Catalytic Performance, and Reaction Mechanisms for Soot Combustion. *ACS Catal.* **2022**, *12*, 15056–15075. [[CrossRef](#)]
39. Yu, X.; Ren, Y.; Yu, D.; Chen, M.; Wang, L.; Wang, R.; Fan, X.; Zhao, Z.; Cheng, K.; Chen, Y.; et al. Hierarchical Porous K-OMS-2/3DOM-m Ti<sub>0.7</sub>Si<sub>0.3</sub>O<sub>2</sub> Catalysts for Soot Combustion: Easy Preparation, High Catalytic Activity, and Good Resistance to H<sub>2</sub>O and SO<sub>2</sub>. *ACS Catal.* **2021**, *11*, 5554–5571. [[CrossRef](#)]
40. Cui, B.; Zhou, L.; Li, K.; Liu, Y.-Q.; Wang, D.; Ye, Y.; Li, S. Holey Co-Ce oxide nanosheets as a highly efficient catalyst for diesel soot combustion. *Appl. Catal. B* **2020**, *267*, 118670. [[CrossRef](#)]
41. Li, Y.; Sun, Q.; Kong, M.; Shi, W.; Huang, J.; Tang, J.; Zhao, X. Coupling Oxygen Ion Conduction to Photocatalysis in Mesoporous Nanorod-like Ceria Significantly Improves Photocatalytic Efficiency. *J. Phys. Chem. C* **2011**, *115*, 14050–14057. [[CrossRef](#)]
42. Zhang, Y.; Zhang, L.; Deng, J.; Dai, H.; He, H. Controlled Synthesis, Characterization, and Morphology-Dependent Reducibility of Ceria–Zirconia–Yttria Solid Solutions with Nanorod-like, Microspherical, Microbowknot-like, and Micro-octahedral Shapes. *Inorg. Chem.* **2009**, *48*, 2181–2192. [[CrossRef](#)] [[PubMed](#)]
43. Niu, F.; Zhang, D.; Shi, L.; He, X.; Li, H.; Mai, H.; Yan, T. Facile synthesis, characterization and low-temperature catalytic performance of Au/CeO<sub>2</sub> nanorods. *Mater. Lett.* **2009**, *63*, 2132–2135. [[CrossRef](#)]
44. Biesinger, M.C.; Payne, B.P.; Grosvenor, A.P.; Lau, L.W.M.; Gerson, A.R.; Smart, R.S.C. Resolving surface chemical states in XPS analysis of first row transition metals, oxides and hydroxides: Cr, Mn, Fe, Co and Ni. *Appl. Surf. Sci.* **2011**, *257*, 2717–2730. [[CrossRef](#)]
45. Galakhov, V.R.; Demeter, M.; Bartkowski, S.; Neumann, M.; Ovechkina, N.A.; Kurmaev, E.Z.; Lobachevskaya, N.I.; Mukovskii, Y.M.; Mitchell, J.; Ederer, D.L. Mn 3s exchange splitting in mixed-valence manganites. *Phys. Rev. B* **2002**, *65*, 113102. [[CrossRef](#)]
46. Yu, D.; Yu, X.; Zhang, C.; Wang, L.; Fan, X.; Zhao, Z.; Wei, Y.; Liu, J.; Gryboš, J.; Leszczyński, B.; et al. Layered Na<sub>2</sub>Mn<sub>3</sub>O<sub>7</sub> decorated by Cerium as the robust catalysts for efficient low temperature soot combustion. *Appl. Catal. B* **2023**, *338*, 123022. [[CrossRef](#)]

47. Hou, J.; Li, Y.; Mao, M.; Ren, L.; Zhao, X. Tremendous Effect of the Morphology of Birnessite-Type Manganese Oxide Nanostructures on Catalytic Activity. *ACS Appl. Mater. Interfaces* **2014**, *6*, 14981–14987. [[CrossRef](#)]
48. Chen, H.; Sayari, A.; Adnot, A.; Larachi, F. Composition–activity effects of Mn–Ce–O composites on phenol catalytic wet oxidation. *Appl. Catal. B* **2001**, *32*, 195–204. [[CrossRef](#)]
49. Cao, C.; Xing, L.; Yang, Y.; Tian, Y.; Ding, T.; Zhang, J.; Hu, T.; Zheng, L.; Li, X. Diesel soot elimination over potassium-promoted  $\text{Co}_3\text{O}_4$  nanowires monolithic catalysts under gravitation contact mode. *Appl. Catal. B* **2017**, *218*, 32–45. [[CrossRef](#)]
50. Yang, Y.; Zhao, D.; Gao, Z.; Tian, Y.; Ding, T.; Zhang, J.; Jiang, Z.; Li, X. Interface interaction induced oxygen activation of cactus-like  $\text{Co}_3\text{O}_4$ /OMS-2 nanorod catalysts in situ grown on monolithic cordierite for diesel soot combustion. *Appl. Catal. B* **2021**, *286*, 119932. [[CrossRef](#)]
51. Weiman, L.; Haidi, L.; Yunfa, C. Mesoporous  $\text{MnO}_x$ – $\text{CeO}_2$  composites for  $\text{NH}_3$ -SCR: The effect of preparation methods and a third dopant. *RSC Adv.* **2019**, *9*, 11912–11921. [[CrossRef](#)] [[PubMed](#)]
52. Wang, B.; Wang, M.; Han, L.; Hou, Y.; Bao, W.; Zhang, C.; Feng, G.; Chang, L.; Huang, Z.; Wang, J. Improved Activity and  $\text{SO}_2$  Resistance by Sm-Modulated Redox of  $\text{MnCeSmTiO}_x$  Mesoporous Amorphous Oxides for Low-Temperature  $\text{NH}_3$ -SCR of NO. *ACS Catal.* **2020**, *10*, 9034–9045. [[CrossRef](#)]
53. Wang, L.; Ren, Y.; Yu, X.; Yu, D.; Peng, C.; Zhou, Q.; Hou, J.; Zhong, C.; Yin, C.; Fan, X.; et al. Facile preparation, catalytic performance and reaction mechanism of  $\text{Mn}_x\text{Co}_{1-x}\text{O}_\delta$ /3DOM-m  $\text{Ti}_{0.7}\text{Si}_{0.2}\text{W}_{0.1}\text{O}_y$  catalysts for the simultaneous removal of soot and  $\text{NO}_x$ . *Catal. Sci. Technol.* **2022**, *12*, 1950–1967. [[CrossRef](#)]
54. Sellers-Antón, B.; Bailón-García, E.; Cardenas-Arenas, A.; Davó-Quñonero, A.; Lozano-Castelló, D.; Bueno-López, A. Enhancement of the Generation and Transfer of Active Oxygen in Ni/ $\text{CeO}_2$  Catalysts for Soot Combustion by Controlling the Ni–Ceria Contact and the Three-Dimensional Structure. *Environ. Sci. Technol.* **2020**, *54*, 2439–2447. [[CrossRef](#)] [[PubMed](#)]
55. Jian, S.; Yang, Y.; Ren, W.; Xing, L.; Zhao, D.; Tian, Y.; Ding, T.; Li, X. Kinetic analysis of morphologies and crystal planes of nanostructured  $\text{CeO}_2$  catalysts on soot oxidation. *Chem. Eng. Sci.* **2020**, *226*, 115891. [[CrossRef](#)]
56. Zhai, G.; Wang, J.; Chen, Z.; Yang, S.; Men, Y. Highly enhanced soot oxidation activity over 3DOM  $\text{Co}_3\text{O}_4$ - $\text{CeO}_2$  catalysts by synergistic promoting effect. *J. Hazard. Mater.* **2019**, *363*, 214–226. [[CrossRef](#)]
57. Wu, X.; Liu, S.; Weng, D.; Lin, F.; Ran, R.  $\text{MnO}_x$ – $\text{CeO}_2$ – $\text{Al}_2\text{O}_3$  mixed oxides for soot oxidation: Activity and thermal stability. *J. Hazard. Mater.* **2011**, *187*, 283–290. [[CrossRef](#)]
58. Yu, X.; Li, J.; Wei, Y.; Zhao, Z.; Liu, J.; Jin, B.; Duan, A.; Jiang, G. Three-Dimensionally Ordered Macroporous  $\text{Mn}_x\text{Ce}_{1-x}\text{O}_\delta$  and Pt/ $\text{Mn}_{0.5}\text{Ce}_{0.5}\text{O}_\delta$  Catalysts: Synthesis and Catalytic Performance for Soot Oxidation. *Ind. Eng. Chem. Res.* **2014**, *53*, 9653–9664. [[CrossRef](#)]

**Disclaimer/Publisher’s Note:** The statements, opinions and data contained in all publications are solely those of the individual author(s) and contributor(s) and not of MDPI and/or the editor(s). MDPI and/or the editor(s) disclaim responsibility for any injury to people or property resulting from any ideas, methods, instructions or products referred to in the content.